



HAL
open science

Vortex-induced vibration prediction via an impedance criterion

Diogo Ferreira Sabino, David Fabre, Justin Leontini, David Lo Jacono

► **To cite this version:**

Diogo Ferreira Sabino, David Fabre, Justin Leontini, David Lo Jacono. Vortex-induced vibration prediction via an impedance criterion. *Journal of Fluid Mechanics*, 2020, 890 (A4), pp.1-22. 10.1017/jfm.2020.104 . hal-02945864

HAL Id: hal-02945864

<https://hal.science/hal-02945864v1>

Submitted on 22 Sep 2020

HAL is a multi-disciplinary open access archive for the deposit and dissemination of scientific research documents, whether they are published or not. The documents may come from teaching and research institutions in France or abroad, or from public or private research centers.

L'archive ouverte pluridisciplinaire **HAL**, est destinée au dépôt et à la diffusion de documents scientifiques de niveau recherche, publiés ou non, émanant des établissements d'enseignement et de recherche français ou étrangers, des laboratoires publics ou privés.



Open Archive Toulouse Archive Ouverte




OATAO is an open access repository that collects the work of Toulouse researchers and makes it freely available over the web where possible

This is an author's version published in: <https://oatao.univ-toulouse.fr/25924>

Official URL:

<https://doi.org/10.1017/jfm.2020.104>

To cite this version:

Ferreira Sabino, Diogo  and Fabre, David  and Leontini, Justin and Lo Jacono, David  *Vortex-induced vibration prediction via an impedance criterion*. (2020) *Journal of Fluid Mechanics*, 890 (A4). 1-22. ISSN 0022-1120.

Any correspondence concerning this service should be sent to the repository administrator: tech-oatao@listes-diff.inp-toulouse.fr

Vortex-induced vibration prediction via an impedance criterion

D. Sabino^{1,†}, D. Fabre¹, J. S. Leontini² and D. Lo Jacono¹

¹Institut de Mécanique des Fluides de Toulouse (IMFT), Université de Toulouse, CNRS, Toulouse, France

²Swinburne University of Technology, Hawthorn, Victoria, 3122, Australia

The vortex-induced vibration of a spring-mounted, damped, rigid circular cylinder, immersed in a Newtonian viscous flow and capable of moving in the direction orthogonal to the unperturbed flow is investigated for Reynolds numbers Re in the vicinity of the onset of unsteadiness ($15 \leq Re \leq 60$) using the incompressible linearised Navier–Stokes equations. In a first step, we solve the linear problem considering an imposed harmonic motion of the cylinder. Results are interpreted in terms of the mechanical impedance, i.e. the ratio between the vertical force coefficient and the cylinder velocity, which is represented as function of the Reynolds number and the driving frequency. Considering the energy transfer between the cylinder and the fluid, we show that impedance results provide a simple criterion allowing the prediction of the onset of instability of the coupled fluid-elastic structure case. A global stability analysis of the fully coupled fluid/cylinder system is then performed. The instability thresholds obtained by this second approach are found to be in perfect agreement with the predictions of the impedance-based criterion. A theoretical argument, based on asymptotic developments, is then provided to give a prediction of eigenvalues of the coupled problem, as well as to characterise the region of instability beyond the threshold as function of the reduced velocity U^* , the dimensionless mass m^* and the Reynolds number. The influence of the damping parameter γ on the instability region is also explored.

Key words: vortex shedding, parametric instability, flow–structure interactions

1. Introduction

Flows over bluff bodies are often encountered in a natural environment as well as in many engineering applications. For the canonical flow past a circular cylinder, it is now well established that the two-dimensional symmetric flow undergoes a global instability at a critical Reynolds number of $Re_c \approx 47$, via a supercritical Hopf bifurcation (Provansal, Mathis & Boyer 1987; Dušek, Le Gal & Frainié 1994). This bifurcation is at the origin of the onset of the time-periodic vortex shedding phenomenon.

† Email address for correspondence: diogo.ferreirasabino@imft.fr

One of the consequences of the vortex shedding phenomenon is the dramatic increase of the drag force, due to the low base pressure on the rear of the body. The unsteadiness in the wake may excite resonant structural vibrations, thus causing fatigue failure, early deterioration of the materials and consequent safety problems. These vibrations are driven by the fluctuations in the lift and drag forces acting on the body surfaces. Consequently, a coupling between the motion of the structure and the flow, commonly referred as fluid–structure interaction or flow-induced vibration, must be taken into account when studying the vortex shedding phenomenon. In particular, when the coupling between the structure and the flow leads to the cylinder oscillating with the same frequency as the vortex shedding, high-amplitude vortex-induced vibration (VIV) occurs. Further details about the VIV phenomenon are given in the reviews of Griffin, Skop & Koopmann (1973), Parkinson (1989) and Williamson & Govardhan (2004).

All these features are fundamentally linked to instability mechanisms that arise above a critical Reynolds number, Re_c , denoted as a supercritical regime, where the coupled fluid–structure system becomes unstable, leading to an unsteady flow.

This instability was previously studied by Cossu & Morino (2000) via a linear stability analysis (LSA) of a system where the cylinder motion was constrained to oscillate only transverse to the free stream (1DOF). This study argued that the critical Reynolds number may decrease to less than a half of the Re_c associated with the fixed-case cylinder, when the mass ratio parameter is small. Subsequently, Buffoni (2003) carried out an experimental study showing that the unsteady vortex shedding could be triggered at Reynolds numbers as low as $Re = 25$ by forcing the cylinder displacement in the crosswise direction (1DOF) at certain frequencies and amplitudes. Later, a transverse and in-line vibration (2DOF) was investigated by Mittal & Singh (2005), showing that vortex shedding and VIV could be found for Reynolds numbers as low as $Re = 20$ for certain values of mass ratio and natural frequency of the coupled spring system. Furthermore, similar conclusions were made by Meliga & Chomaz (2011) using a 2DOF asymptotic expansion approach and by Zhang *et al.* (2015) using a 1DOF reduced-order model approach. Subsequently, a study of the lock-in regime (match of the wake vortex mode and body oscillation frequencies) was conducted by Navrose & Mittal (2016) using a 1DOF global LSA, and the subcritical regime of the 1DOF cylinder was studied by Kou *et al.* (2017) using a dynamic mode decomposition.

The forced cylinder configuration, where the motion of the body is externally controlled, has also been extensively studied. The pioneering work on this area was first accomplished by Bishop & Hassan (1964) and Feng (1968). This work was followed by the investigations of Williamson & Roshko (1988) where the ‘lock-in’ regions are studied. Karniadakis & Triantafyllou (1989) also studied a forced cylinder configuration at low supercritical Reynolds numbers. The connection between the coupled and forced configuration has also been investigated, for example, in Morse & Williamson (2006), Morse & Williamson (2009a) and Morse & Williamson (2009b). A review on vortex-induced vibrations of isolated circular cylinders was presented in Bearman (2011).

This study is presented in the framework of hydrodynamic instabilities, with the focus on the characterisation of the flow behaviour by a global linear stability approach at a Reynolds number, Re , near the bifurcation where the flow transits from a steady equilibrium state to an unsteady periodic state. When cylinder displacement is allowed, this phenomenon no longer occurs at $Re_c \approx 47$. Instead, the bifurcation is expected to occur at lower Re and can possibly be triggered by a different mechanism from the classical one encountered in the fixed cylinder case.

The objective of the present study is to fully characterise this transition for a spring-mounted cylinder and predict it with an impedance criterion, as well as to use an asymptotic development based on the forced case to predict the eigenvalue behaviour of the coupled case for both subcritical and supercritical regimes, i.e. cases at Re below and above the threshold value. Recently, a similar reasoning based on the acoustic impedance was also successfully applied to the oscillating flow through a circular hole in a thick plate Fabre *et al.* (2020).

The cylinder instability is therefore first investigated by analysing the case where the cylinder is forced to oscillate sinusoidally transverse to the free stream direction for Reynolds numbers $15 < Re < 60$. The results are then treated in terms of the impedance, the ratio between the vertical force coefficient and the cylinder velocity. The impedance is closely related to the definition of energy transfer between the fluid and the cylinder, enabling the forced and coupled cases to be linked at the marginal energy transfer point and in its vicinity. Following this, the coupled case is analysed, by modelling the 1DOF motion with a damped spring–mass equation. Linear stability analysis is carried out around the steady equilibrium state, and the stability of this state is determined based on the eigenvalues of the linearised problem for several (Re, m^*, U^*, γ) arrangements. The results of the coupled case are then compared with the impedance-based predictions from the forced case, both for subcritical and supercritical flow regimes.

2. Mathematical formulation

2.1. Fluid formulation

A Cartesian coordinate system is used with its origin at the centre of the cylinder, which travels with the cylinder motion. The \hat{i} -axis is considered parallel to the streamwise direction, whereas the \hat{j} -axis points laterally, as depicted in figure 1(a). The spatial and temporal domains are represented by $\Omega \in \mathbb{R}^2$ and $[0, T]$, respectively. Following the formulation of Mougin & Magnaudet (2002), which consists of expressing the absolute velocity \mathbf{u} in the relative frame moving with the cylinder, the flow around the cylinder can be described by the non-dimensional laminar incompressible Navier–Stokes equations, defined as

$$\partial_t \mathbf{u} + ((\mathbf{u} - \dot{\zeta} \hat{\mathbf{j}}) \cdot \nabla) \mathbf{u} = -\nabla p + 2Re^{-1} \nabla \cdot \mathbf{D}(\mathbf{u}), \quad (2.1a)$$

$$\nabla \cdot \mathbf{u} = 0, \quad (2.1b)$$

on $\Omega \times [0, T]$, where $\mathbf{D}(\mathbf{u}) \stackrel{\text{def}}{=} 1/2(\nabla \mathbf{u} + \nabla \mathbf{u}^T)$ is the rate-of-strain tensor, p the static pressure, ρ_f the fluid density and ζ the instantaneous cylinder displacement. The Reynolds number Re is defined as $Re = DU_\infty/\nu$, where D is the cylinder diameter, U_∞ the upstream unperturbed velocity and ν the kinematic viscosity.

The domain limits are depicted in figure 1(b). To take advantage of the problem's symmetry, a half-domain representation is implemented with the proper boundary conditions on the axis in order to obtain the symmetric or anti-symmetric (periodic) solutions. The remaining boundary conditions are posed as

$$\mathbf{u} = -\dot{\zeta} \hat{\mathbf{j}} \quad \text{on } \Gamma_{cy}, \quad (2.2a)$$

$$\mathbf{u} = U_\infty \hat{\mathbf{i}} \quad \text{on } \Gamma_{in} \cup \Gamma_{lat}, \quad (2.2b)$$

$$[-\nabla p + 2Re^{-1} \mathbf{D}(\mathbf{u})] \cdot \mathbf{n} = 0 \quad \text{on } \Gamma_{out}, \quad (2.2c)$$

with \mathbf{n} the outward unit normal to the boundary.

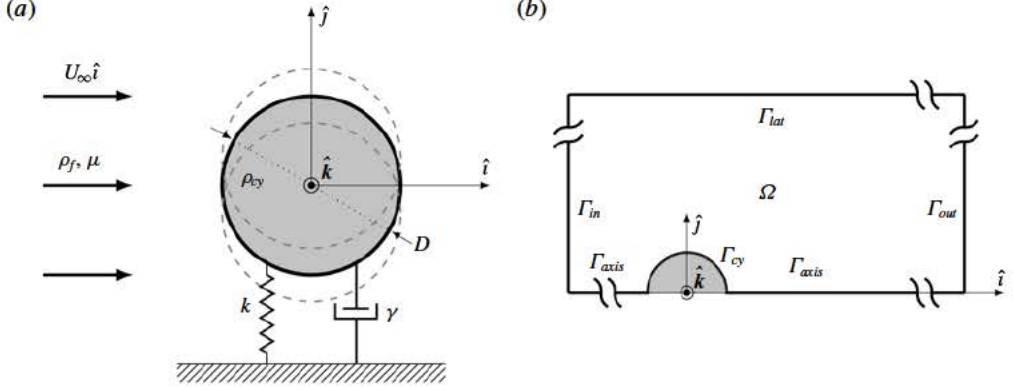


FIGURE 1. (a) A schematic showing the dimensional input variables of the damped spring–mass cylinder and the coordinate system of the problem, and (b) a schematic representation of the computational domain and boundary conditions.

2.2. Structure model: forced and coupled formulations

The effect of the motion of the cylinder on the fluid flow appears through the transverse velocity $\dot{\zeta}(t)$ of the cylinder which is present in both the Navier–Stokes equations (2.1) and the boundary condition (2.2a).

For the forced case, the displacement is imposed by a sinusoidal motion under the form $\dot{\zeta} = |\dot{\zeta}_F| \sin(\omega_F t)$, where ω_F is the imposed frequency.

For the coupled case, the linear equation modelling the motion of the cylinder is posed as

$$\ddot{\zeta} + \frac{4\pi\gamma}{U^*} \dot{\zeta} + \left(\frac{2\pi}{U^*}\right)^2 \zeta = \frac{2C_y(t)}{\pi m^*}, \quad (2.3)$$

where γ is the damping ratio, $m^* = \rho_{cy}/\rho_f$, is the mass ratio between the cylinder and fluid densities, $U^* = U_\infty/(f_N D) = 2\pi U_\infty \sqrt{m_{cy}/k}/D$ is the reduced velocity and $C_y(t) = F_y(t)/(0.5\rho U_\infty^2 D)$ is the vertical force coefficient, where m_{cy} and k are the cylinder mass and the spring stiffness, respectively, and $F_y(t)$ is the vertical force. The latter is calculated by integrating the stress on the boundary of the cylinder

$$C_y(t) = \frac{2F_y(t)}{\rho U_\infty^2 D} = 2 \int_{\Gamma_{cy}} 2\{(-pn + 2Re^{-1} \mathbf{D}(\mathbf{u}) \cdot \mathbf{n}) \cdot \hat{\mathbf{j}}\} d\Gamma_{cy}, \quad (2.4)$$

where the factor 2 accounts for the fact that a half-domain is used.

2.3. Linearised Navier–Stokes equations

In the framework of linearised Navier–Stokes equations, the fluid flow, denoted $\mathbf{q} = (\mathbf{u}, p)^T$, is decomposed as

$$\mathbf{q} = \mathbf{q}_b + \frac{\epsilon}{2} (\hat{\mathbf{q}} e^{-i\omega t} + \text{c.c.}), \quad (2.5)$$

where $\mathbf{q}_b = (\mathbf{u}_b, p_b)^T$ is the steady base flow, ϵ is a small parameter, $\hat{\mathbf{q}}$ is the perturbation in an ‘eigenmode form’ with c.c. standing for the complex conjugate and

ω is the complex eigenvalue. The base flow \mathbf{q}_b is the solution of the time-independent version of the Navier–Stokes equations, which are detailed in appendix B.

Similarly, the cylinder velocity $\dot{\zeta}(t)$ and the dimensionless force $C_y(t)$ will be expressed under the same ‘eigenmode form’

$$\dot{\zeta}(t) = \epsilon \frac{\hat{\zeta} e^{-i\omega t} + \text{c.c.}}{2}, \quad C_y(t) = \epsilon \frac{\hat{C}_y e^{-i\omega t} + \text{c.c.}}{2}. \quad (2.6a,b)$$

The eigenmode ansatz (2.5) and (2.6) will be used for both the forced and the coupled problems, so that a difference in the ω can be interpreted as follows.

- (i) For the forced problem, ω is the frequency of the imposed motion of the cylinder and will generally be considered as real (and noted $\omega \equiv \omega_F$).
- (ii) For the coupled problem, on the other hand, ω is the eigenvalue and is generally expected to be a complex number ($\omega = \omega_r + i\omega_i$). Note that the imaginary part ω_i corresponds to the amplification rate, and its sign defines whether the solution decays or grows over time, representing a stability criterion of the eigenmode.

2.3.1. Linearised forced problem

For the forced problem, $\hat{\mathbf{q}}$ will be noted $\hat{\mathbf{q}}_F$ and the linearised Navier–Stokes equations can be set under the following form:

$$(\mathbf{A}_{ff} - i\omega_F \mathbf{B}_{ff}) \hat{\mathbf{q}}_F = \hat{\zeta}_F \mathbf{Y}, \quad (2.7)$$

where \mathbf{A}_{ff} and \mathbf{B}_{ff} are the fluid and mass operators and the operator \mathbf{Y} represents the effect of the cylinder motion on the fluid (which appears both as a volumetric term in the Navier–Stokes equations and in the boundary conditions). The weak form expressions for these operators are given in appendix B.

Once this problem is solved, the vertical force coefficient can be extracted as $\hat{C}_y = \mathbf{L}(\hat{\mathbf{q}}_F)$ where \mathbf{L} is the ‘vertical force coefficient’ operator, also defined in appendix B. The mechanical impedance $Z(\omega_F)$ can now be defined as the ratio between vertical force coefficient amplitude and the cylinder velocity amplitude

$$Z(\omega_F) = -\frac{\hat{C}_y}{\hat{\zeta}} = \frac{\hat{C}_y}{i\omega_F \hat{\zeta}}. \quad (2.8)$$

As shown in the next sections, the concept of impedance provides a useful way to characterise the problem in both the forced case and the coupled case. Moreover, it provides a link with problems in electricity and acoustics where such a concept is widely used. In particular, the real and imaginary part of the impedance ($Z = Z_r + iZ_i$) can be identified with the resistance and reactance, respectively.

Note that, for the forced case, the mechanical impedance can be formally defined as $Z(\omega_F) = -\mathbf{L}(\hat{\mathbf{q}}_F)[(\mathbf{A}_{ff} - i\omega_F \mathbf{B}_{ff}) \hat{\mathbf{q}}_F]^{-1} \cdot \mathbf{Y}$, so the computation of this quantity after discretisation of the operators is straightforward.

2.3.2. Linearised coupled problem

In the coupled problem, the one-way coupling between fluid and the cylinder structure is still represented by (2.7) (with a generally complex ω instead of the real ω_F), but the cylinder displacement $\hat{\zeta}$ is now related to the vertical force coefficient \hat{C}_y through the dynamical equation (2.3). The whole set of equations can now be

written in eigenvalue form considering the state vector $\hat{\mathbf{q}}_{CP} = (\hat{q}, \hat{\zeta}, \dot{\hat{\zeta}}, \ddot{\hat{\zeta}})^T$ as follows:

$$(\mathbf{A} - i\omega\mathbf{B})\hat{\mathbf{q}}_{CP} = \mathbf{0}, \quad (2.9)$$

with

$$\mathbf{A} = \begin{bmatrix} \mathbf{A}_{ff} & 0 & -\mathbf{Y} & 0 \\ 0 & 0 & 1 & 0 \\ 0 & 0 & 0 & 1 \\ \frac{2}{\pi m^*} \mathbf{L} & -\left(\frac{2\pi}{U^*}\right)^2 & -\frac{4\pi\gamma}{U^*} & -1 \end{bmatrix} \quad \text{and} \quad \mathbf{B} = \begin{bmatrix} \mathbf{B}_{ff} & 0 & 0 & 0 \\ 0 & 1 & 0 & 0 \\ 0 & 0 & 1 & 0 \\ 0 & 0 & 0 & 0 \end{bmatrix}. \quad (2.10a,b)$$

3. Energy considerations

3.1. Linking energy transfer and impedance

Following the work done by Morse & Williamson (2009b) and Navrose & Mittal (2016), the net energy transfer from the fluid to the cylinder, over a period T , can be defined as

$$E_{transfer} = \int_0^T [C_y(t)\dot{\zeta}(t)] dt. \quad (3.1)$$

Considering a forced problem (with a real ω_F) with displacement $\zeta(t)$ and dimensionless force $C_y(t)$ given by (2.6), the integration over one period ($T = 2\pi/\omega_F$) leads to (see appendix A)

$$E_{transfer} = -\pi|\hat{\zeta}|^2\omega_F Z_r(\omega_F). \quad (3.2)$$

The property of $E_{transfer}$ being positive for some real value of ω_F has been proposed by Morse & Williamson (2009b) as an instability criterion for the fully coupled problem. This criterion is usually expressed in terms of the phase shift ϕ between the vertical force coefficient and the cylinder displacement

$$E_{transfer} > 0 \iff \phi = \arg(\hat{C}_y/\hat{\zeta}) \in [0, \pi]. \quad (3.3)$$

The concept of impedance introduced in the previous section, allows to express this instability criterion in an alternative form

$$E_{transfer} > 0 \iff Z_r(\omega_F) < 0 \quad \text{for some real } \omega_F. \quad (3.4)$$

This second expression makes sense when recalling that the real part of the impedance is analogous to an electrical resistance; indeed the possibility of negative resistance is a well known source of instability in electrical circuits (see Conciauro & Puglisi 1981).

3.2. Link between forced and coupled problems

Although the criterion discussed in the previous section is physically intuitive, it is not totally rigorous as it uses the impedance computed for some real frequency ω_F to predict an instability, which corresponds to a solution of the coupled problem with some complex ω . The situation can be clarified when considering the impedance

defined by (2.8) as an analytical function of the complex variable ω . Plugging this definition into the dynamical equation (2.3) leads to the following expression:

$$-\omega^2 - \frac{4\pi\gamma i\omega}{U^*} + \left(\frac{2\pi}{U^*}\right)^2 - \frac{2i\omega Z(\omega)}{\pi m^*} = 0. \quad (3.5)$$

Mathematically, the eigenvalues of the coupled problem (2.9) correspond to the complex zeros of this constitutive relation. The objective of this section is to derive a prediction of these eigenvalues as a function of the most easily computed and physically meaningful values of Z along the real ω -axis (i.e. based on the forced problem).

We first note that a condition for the existence of purely real solutions of the relation (3.5) is that the damping rate is zero ($\gamma = 0$) and the impedance is purely imaginary ($Z_r = 0$). This leads to the assumption of the existence of nearly real solutions in the asymptotic limit corresponding to the following hypotheses:

$$|Z_r| \ll |Z_i|, \quad (3.6a)$$

$$\gamma \ll 1. \quad (3.6b)$$

Under these hypotheses it is relevant to look for nearly real eigenvalues with the form

$$\omega = \omega_F + \omega^{(1)}, \quad \text{with } |\omega^{(1)}| \ll |\omega_F| \text{ and } \omega_F \in \mathbb{R}. \quad (3.7)$$

Introducing these hypotheses into equation (3.5) and performing a Taylor development in terms of the quantities assumed small leads to

$$\begin{aligned} & \left[-\omega_F^2 + \left(\frac{2\pi}{U^*}\right)^2 + \frac{2\omega_F Z_i(\omega_F)}{\pi m^*} \right] \\ & + \left[-2\omega_F \omega^{(1)} - \frac{4\pi\gamma i\omega_F}{U^*} + \frac{2\omega_F}{\pi m^*} \left(-\frac{\partial Z}{\partial \omega} \Big|_{\omega=\omega_F} i\omega^{(1)} - iZ_r(\omega_F) + \frac{Z_i(\omega_F)\omega^{(1)}}{\omega_F} \right) \right] \\ & + h.o.t. = 0, \end{aligned} \quad (3.8)$$

where *h.o.t.* denotes the higher-order terms neglected in the development. Inspection of this expression leads to the following conclusions.

- (i) Firstly, the leading-order term (term in the first line) defines an implicit, and possibly multivalued expression when considering ω_F as a function of U^* and m^* . However, it is explicit and particularly simple when solving for U^* in terms of ω_F and m^* ,

$$U^* = \sqrt{\frac{4\pi^2}{\omega_F \left(\omega_F - \frac{2}{\pi m^*} Z_i(\omega_F) \right)}}. \quad (3.9)$$

- (ii) Secondly, the first-order term (term in the second line) leads to an explicit expression for the first-order correction to the frequency $\omega^{(1)}$ as follows:

$$\omega^{(1)} = -i \frac{Z_r(\omega_F) + \frac{2\pi^2\gamma m^*}{U^*}}{\pi m^* - \frac{Z_i(\omega_F)}{\omega_F} + i \frac{\partial Z}{\partial \omega} \Big|_{\omega=\omega_F}}. \quad (3.10)$$

The imaginary part of this expression directly provides an estimation of the growth rate as function of γ , m^* and U^* (using the implicit definition of ω_F given by (3.9)).

The condition on the imaginary part of the frequency, $\text{Im}(\omega^{(1)}) > 0$, thus provides an improved version of the instability criterion compared to the one discussed in the previous subsection, equation (3.4). One can note that in the absence of damping ($\gamma = 0$), the criterion reduces to $Z_r(\omega_F) < 0$ provided that the real part of the denominator is positive. As it will be seen in § 6.3, if this latter term changes sign, the asymptotic prediction may lead to erroneous predictions, but the latter are easily identified as being out of the range of application of the asymptotic theory.

4. Numerical formulation

The numerical approach is based on a finite element method. All the equations solved in the paper are first rewritten in a variational formulation and then spatially discretised via a Delaunay–Voronoi algorithm, generating an unstructured triangular mesh, adapted with an automatic procedure to a given field. This adaptation relies on the AdaptMesh procedure of the FreeFem++ software (see, for instance Hecht (2012)). An adaptation via the structural sensitivity (Giannetti & Luchini 2007), calculated via the solutions of the direct and adjoint eigenproblems (see Fabre *et al.* 2018) was used, in order to adequately discretise the wake region in the rear of the cylinder. The mesh validation for the same configuration is detailed in Fabre *et al.* (2018).

The unknown velocity and pressure fields (\mathbf{u} , p) were spatially discretised using the classical Taylor–Hood basis (\mathcal{P}^2 , \mathcal{P}^2 , \mathcal{P}^1) in order to satisfy the Ladyzhenskaya–Babuška–Brezzi (known as LBB) condition (see, for instance, Brezzi & Fortin (1991)). All the discrete matrices resulting from the projection of the variational formulations onto the basis of finite elements were built with the FreeFem++ software and handled using the MUMPS library, performing a direct LU inversion. The loop over the parameters and data treatment were performed using the Matlab drivers of the StabFem project (<https://gitlab.com/stabfem/StabFem>).

For the forced regime system described in (2.7), the solution is readily computed by inverting the matrix system and multiply it by the forcing term. On the other hand, the linear stability problem results in a generalised eigenvalue problem, which was solved via a shift-and-invert method, a particular case of the Arnoldi method. This strategy allows eigenvalues to be obtained in the vicinity of some given complex shift. Influence of the choice on the adaptation field (and therefore spatial resolution), confinement due to the domain size and sensitivity to the boundary conditions has already been reported in Fabre *et al.* (2018).

5. Linear forced results

5.1. Validation

The results for the linear forced case, described in the following, are treated in terms of the real and imaginary parts of the impedance $Z(\omega_F)$ as a function of the prescribed oscillation frequency represented by the Strouhal number $St_F = \omega_F D / (2\pi U_\infty)$ (see figure 2). For validation the linear forced results are compared to fully nonlinear direct numerical simulations (DNS) performed using a spectral-element code. This method is described in detail in Karniadakis & Sherwin (2005), and the implementation used here follows that described in Thompson, Hourigan & Sheridan (1996). Previous

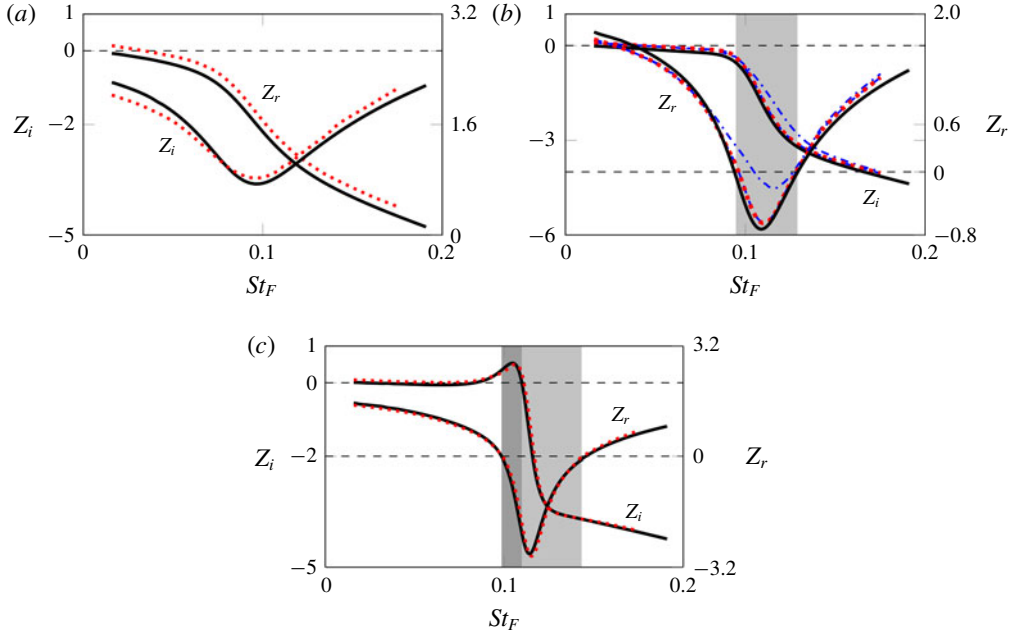


FIGURE 2. Components of the impedance as a function of the imposed oscillation frequency for (a) $Re = 15$, (b) $Re = 25$ and (c) $Re = 35$. Linear forced results are shown with a solid black line (—), as well as DNS results for $|\zeta_F| = 0.2$ (dotted-dashed blue line - · - · -), $|\zeta_F| = 0.02$ (dashed blue line ---) and $|\zeta_F| = 0.002$ (dotted red line · · · · ·). The convergence of the DNS results to the linear results with decreasing amplitude is clear for the $Re = 25$ case shown in (b). The light and dark grey zones represent the first and second instability zones, respectively, according to the Nyquist arguments.

studies using this code for oscillating and coupled vibrating cylinders include Leontini *et al.* (2006a), Leontini, Thompson & Hourigan (2006b) and Leontini *et al.* (2018).

The main parameter that dictates the validity of the comparison between the linear and nonlinear results is the amplitude of the imposed oscillation, which must be small enough to respect the linear hypothesis. The comparison between different imposed amplitudes for the same range of St_F at $Re = 25$ is presented in figure 2(b), for $Z_r(\omega_F)$ and $Z_i(\omega_F)$. As the amplitude decreases, the DNS solution approaches the linear solution. The results for the two smaller amplitudes give almost the same results, confirming that the considered displacement amplitude is small enough. Another two DNS simulations were carried out at $Re = 15$ and $Re = 35$ for $|\zeta_F| = 0.002$. Further, one can see from the plotted data that as Re increases, the DNS results tend to more accurately match the linear forced results.

5.2. Instability thresholds established using linear forced oscillations

A presentation of the main results for the linear forced case can be seen in figures 2 and 3(a). The latter sketches the results in a Nyquist diagram (Z_r versus Z_i). Two instability zones are highlighted and discussed in the following paragraphs.

The first interesting phenomenon occurs at $Re = Re_{c1} = 19.915$ (shown with the solid green curve, figure 3a) where the sign of Z_r first becomes negative at $St_{F,c1} = 0.104$, indicating a positive energy transfer from the fluid to the cylinder. The limit condition

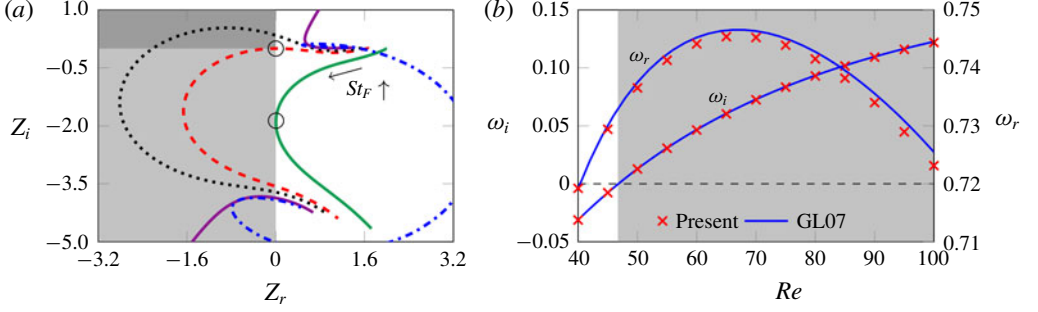


FIGURE 3. (a) A Nyquist diagram plotting the real and imaginary components of the impedance for the forced results. Each curve represents a constant Re , St_F progresses along the curve. Values of Re are: $Re = 19.915 = Re_{c1}$ (solid green line —); $Re = 30.349 = Re_{c2}$ (dashed red line - - - -); $Re = 35$ (dotted black line - - - -); $Re = 46.766 = Re_{c3}$ (solid violet line —); $Re = 55$ (dotted-dashed blue line - · - · -). The light and dark grey zones represent the first and second instability zones, respectively. (b) A comparison of the eigenvalues calculated from the coupled case for the fluid mode (FM) for $U^* \rightarrow 0$ at $m^* = 1000$, and those from the fixed-case cylinder (from Giannetti & Luchini (2007) noted GL07). The grey zone represents the unstable region.

can be written as

$$\text{At } Re = Re_{c1}, \quad \exists St_F \in \mathbb{R}^+ \mid Z_r(St_F) = 0, \quad (5.1)$$

and this is represented on the plot as the lighter grey region.

The second interesting phenomenon occurs at $Re = Re_{c2} = 30.349$ (shown with the dashed red curve, figure 3a) with the curve that passes exactly through the origin of the Nyquist diagram, indicating that a forcing frequency exists where the impedance is exactly zero. The limit condition for this point can be written as

$$\text{At } Re = Re_{c2}, \quad \exists St_F \in \mathbb{R}^+ \mid Z(St_F) = 0, \quad (5.2)$$

and the region where simultaneously Z_r is negative and Z_i is positive is represented by the darker grey region. The classical Nyquist criterion then states that this value of Re_{c2} presents a lower bound for values of Re that can produce a positive value of Z_i – for values of Re beyond this, the Nyquist curve will encircle the origin in an anticlockwise direction. An upper bound exists for this behaviour, Re_{c3} , which is explained below. Physically, the condition $Z(St_F) = 0$ implies that there exists a solution of the linearised problem in which the value of $C_{y,F}$ is zero and therefore, following equation (3.1), the energy transfer between the forced case cylinder and the flow will also be zero.

The third critical phenomenon occurs at $Re = Re_{c3} = 46.766$ (shown with the solid purple curve, figure 3a). At this Re the steady base flow becomes hydrodynamically unstable. This means that perturbations are expected to grow even in the absence of any forcing, i.e. at a certain St_F one will have $Z(St_F) \rightarrow \infty$ and therefore $\hat{\zeta} \rightarrow 0$. One observes that the curve tends to infinity, with the limit condition written as

$$\text{at } Re = Re_{c3}, \quad \exists St_F \in \mathbb{R}^+ \mid Z(St_F) = \infty. \quad (5.3)$$

For $Re > Re_{c3}$, the flow is predicted to be unsteady, regardless of the frequency and energy transfer characteristics of a small-amplitude harmonic forcing.

So, the results presented in the Nyquist diagram of figure 3(a) can be interpreted as follows. For $Re \geq Re_{c1} = 19.915$, there is a range of forcing frequencies which results in a positive energy transfer to the cylinder and therefore the flow is predicted to be unstable. For $Re \geq Re_{c2} = 30.349$, there is a range of forcing frequencies that produce a positive imaginary component of the impedance Z_i within the unstable zone $Z_r < 0$. For $Re > Re_{c3} = 46.766$, the flow is unstable regardless of the form of any linear forcing.

6. Linear results for the coupled problem

The results for the coupled problem, described in the following, are analysed in terms of the eigenvalue ω and its variation with the problem's parameters, (Re, m^*, U^*, γ) . The value of the damping ratio γ will be considered to be zero throughout the following analysis, with the exception of § 6.6. The impedance-based predictions from the forced case at the leading order and at the first order are compared with the results of the LSA both for subcritical and supercritical regimes.

6.1. Eigenmode classification and behaviour

As reported in Cossu & Morino (2000), Meliga & Chomaz (2011) and Navrose & Mittal (2016) (the latter will hereinafter be denoted as NM16), the coupled transverse cylinder motion introduces two complex-conjugate eigenvalues to the physical spectrum and therefore two eigenmodes, referred to as a fluid mode and a structural mode (EM), as proposed in NM16. This is in contrast to the fixed case, where only FM can be found.

The classification of the two modes found in the coupled moving cylinder case is divided according to their nature and relation. This identification is based on the eigenmode characteristics in the limit of very large m^* since for this case, the flow-induced vertical force becomes very small compared with the structural ones and the fluid–structure interaction drops to negligible levels (Meliga & Chomaz 2011).

On one hand, the real part of the eigenvalue associated with the EM tends to the natural angular frequency of the cylinder system, i.e. $2\pi/U^* \equiv \omega_N$ and the mode behaves similarly to a cylinder oscillating *in vacuo*. Further, the imaginary part of the eigenvalue tends to zero, matching this latter behaviour.

On the other hand, the eigenvalue associated with the FM tends to the leading eigenvalue computed for the fixed case, i.e. the mode behaves similarly to the modes in the fixed cylinder case.

However, for relatively low m^* the distinction between FM and EM is not possible, since eigenvalues may coalesce for certain combinations of (Re, U^*, m^*) , especially for lower m^* or when $Re \rightarrow 46.7$. The two leading eigenmodes do not exhibit a clear distinction in terms of their affiliation to being either a FM or a EM. They are therefore referred as coupled modes and, following NM16 nomenclature, they are denoted as fluid-elastic mode 1 (FEM1) and fluid-elastic mode 2 (FEM2). Further at $Re \geq Re_{c3}$, for small U^* , the FEM1 resembles to the FM, whereas the FEM2 is similar to the EM. However, for large U^* , the characteristics of FEM1 and FEM2 resemble the EM and the FM, respectively. For $Re \leq Re_{c3}$, the inverse reasoning can be applied and can easily be confirmed in the figures of the following sections.

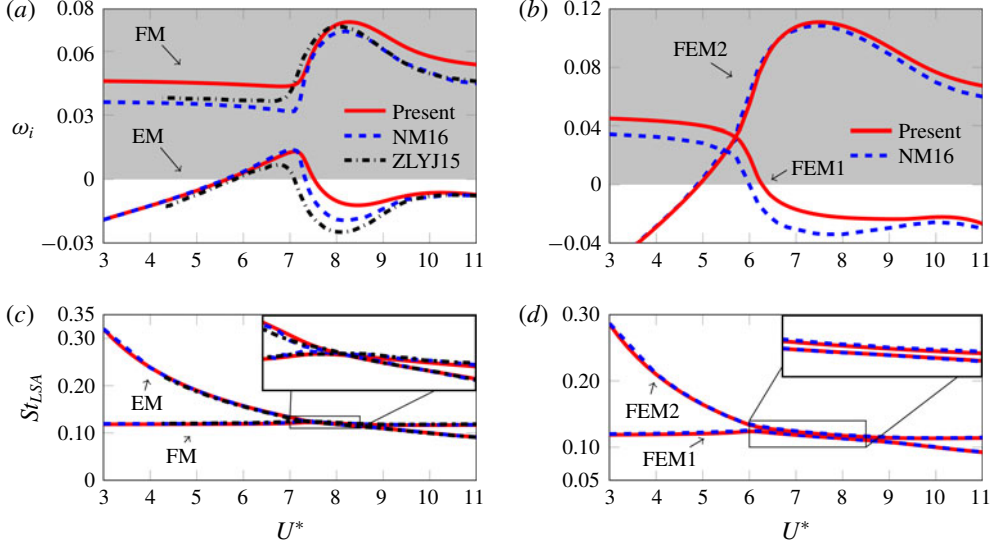


FIGURE 4. Linear stability results: real and imaginary parts of the eigenvalue ω with U^* at $Re = 60$ for $m^* = 20$ (a,c) and $m^* = 5$ (b,d). The zoom in the frequency plots ((c) and (d)) shows that the curves cross each other for $m^* = 20$ but not for $m^* = 5$. The grey zone represents the unstable region.

6.2. Validation

The validation of the results is first done by comparing the results with the fixed-case cylinder, a classical case of hydrodynamic instability. For that purpose, results are obtained for $U^* \rightarrow 0$. This asymptotic approach constrains the spring stiffness to large values, $k \rightarrow \infty$ while m^* remains finite. It is first noted that the real part of the eigenvalue associated with the EM tends to infinity, for all Re , as expected for the natural frequency of the structure-only system, $2\pi/U^*$. These singularity configurations were intensively studied in Fabre, Assemat & Magnaudet (2011). The attention of the present study is rather focused on the behaviour of the FM. The imaginary and real parts of the eigenvalue associated with the FM show a good agreement when compared with the fixed case results, reported in Giannetti & Luchini (2007), as shown in figure 3(b).

The results are also compared with data from NM16 and from Zhang *et al.* (2015) (hereinafter denoted as ZLYJ15). Figure 4 shows the real and imaginary parts of the eigenvalue variation as a function of $U^* = [3, 11]$ for $Re = 60$ and $m^* = \{5, 20\}$. Real parts are sketched in terms of $St_{LSA} = \omega_r/2\pi$. One can notice that the St_{LSA} associated with the FM remains nearly constant, similar to the St_{LSA} associated with the fixed case, for all values of U^* . Further, one notes that the growth rate of the most unstable mode is maximum within the U^* range where the frequencies of the two modes are close to each other. This is observed both in this case as in the following ones in the next sections. While the real part presents no difference when comparing the present study and the cited references, the imaginary part of the eigenvalue shows a discrepancy between all sources. Although there is a qualitative match of the results, their values do not agree. However, the present study shows an ω_i at $U^* = 3$ that is close to the fixed-case cylinder value for the same Re , depicted in figure 3(b), although this is not verified by the values from NM16 or ZLYJ15. Further, the present

LSA results are compared with the impedance-based predictions in the next section, showing a good agreement where the asymptotic theory is valid.

One of the possible causes associated with these differences could be the computational resolution. On one hand, NM16 used a stabilised finite element method based on streamline-upwind/Petrov–Galerkin (known as SUPG) and pressure-stabilizing/Petrov–Galerkin (known as PSPG) techniques (Navrose & Mittal 2016). On the other hand, ZLYJ15 used a reduced-order model of the unsteady Navier–Stokes equations in a finite-volume formulation coupled with the structural motion equations. Both methods differ from that implemented here and could be the cause of the discrepancy. Since the influence of the mesh refinement, boundary conditions and domain size was already explored in the present investigation (see Fabre *et al.* 2018), the latter does not seem to be the source of error.

It is clear that, for $Re = 60$, an eigenvalue for which ω_i is positive will always exist at any reduced velocity. For the purpose of identifying the stable and unstable zones, a different analysis was carried out at lower Re values which is explored in §§ 6.4 and 6.5.

6.3. Comparison with impedance-based asymptotic predictions

The eigenvalues computed by resolution of the coupled eigenvalue problem are compared with the asymptotic predictions of § 3.2 in figure 5. Figure 5(a) considers the case $Re = 60$, $m^* = 20$. In this case, already considered in figure 4(a,c), the FM and the EM are distinct, and the asymptotic prediction accurately follows the eigenvalue of the EM. For $Re = 60$, $m^* = 5$ (figure 5b), a situation close to that in figure 4(b,d) and characterised by coupled modes FEM1 and FEM2, it is observed that the asymptotic prediction first follows the FEM2 branch and then abruptly switches to the FEM1 branch. The same pattern is observed for $Re = 60$, $m^* = 0.1$ (figure 5c), but the asymptotic prediction displays an abrupt behaviour at the transition, which does not fit with the stability results. Still, the prediction correctly reproduces the behaviour in the vicinity of the thresholds.

Consider now the situation for $Re = 42$, a value located below the threshold $Re_{c3} \approx 46.7$. In this case, numerical results only provide a single unstable eigenmode (noted EM or FEM2), and a stable mode (noted FM, when corresponding to the fluid, or FEM1). For $m^* = 20$ (figure 5d), the impedance-based prediction asymptotically fits the EM branch around the linearisation value. Note that in this case, the $\omega_F - U^*$ relation defined by (3.9) is multivalued in the range $U^* \in [9.640 - 9.729]$. The zoom detail in the figure shows that the asymptotic prediction still correctly fits in the vicinity of the neutral curve but quickly departs from it.

The case $Re = 42$, $m^* = 5$ (figure 5e) is even more complicated. In this case, the asymptotic prediction is multivalued in the range $U^* \in [10.478 - 16.147]$ and the corresponding amplification rate crosses the horizontal axis four times (identified with circles in the figure). The results obtained by resolution of the coupled eigenvalue problem are comparatively much simpler, with a single unstable FEM2 branch in the range $U^* \in [5.304 - 11.043]$. Note that both these values are correctly predicted by the asymptotic analysis. On the other hand, the thresholds predicted by the asymptotic prediction at $U^* = 10.539$ and $U^* = 16.110$ do not fit with any results. Inspection shows that these values correspond to a change of sign of the real part of the denominator in (3.10), while the numerator Z_r is large. Hence, in these ranges the asymptotic prediction is used far away from its starting hypothesis in (3.6), which explains why it does not fit with any physical results.

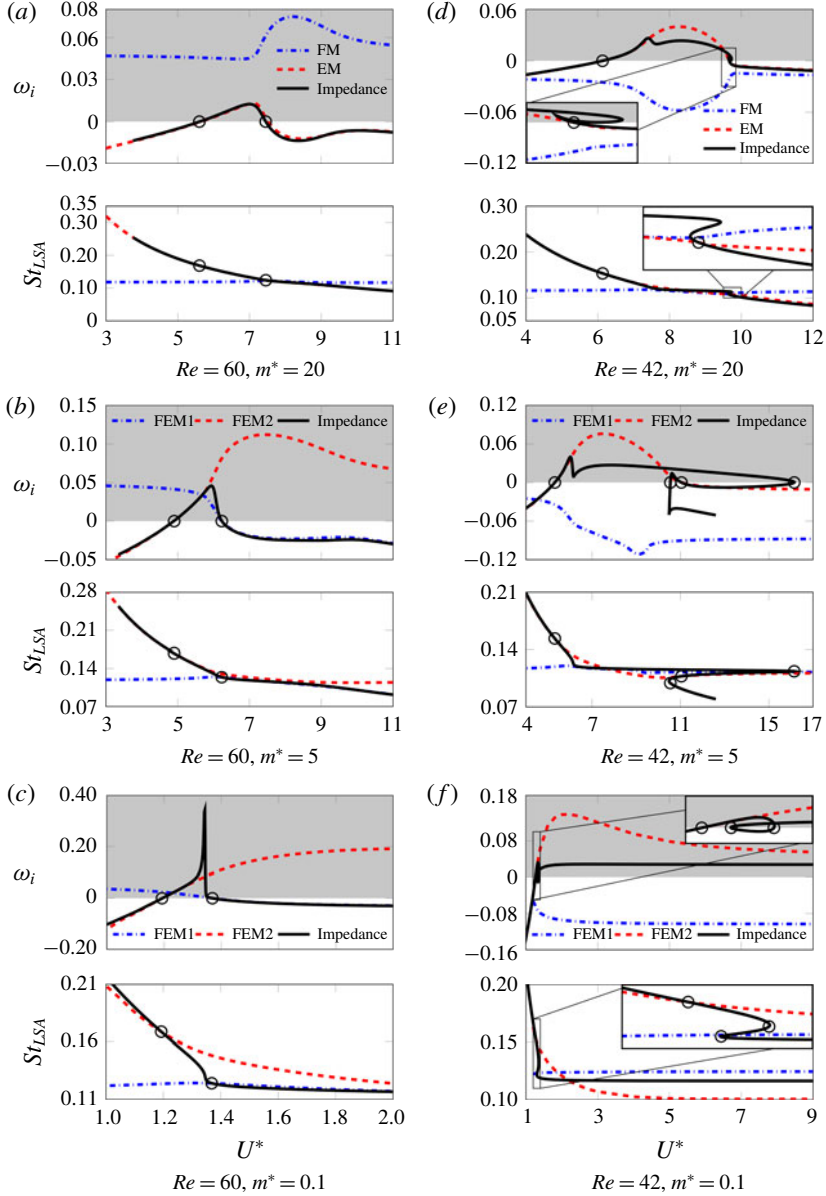


FIGURE 5. Real and imaginary parts of the eigenvalue ω with U^* for $Re = 60$ (a–c) and $Re = 42$ (d–f) for the linear stability analysis of the coupled problem and the impedance-based asymptotic predictions based on the forced problem. The grey zone represents the unstable region.

Finally, for $Re = 42, m^* = 0.1$ (figure 5f) the numerically computed branch FEM2 is unstable in the range $U^* \in [1.270 - \infty]$. Note that in this case there is no upper threshold for restabilisation. The asymptotic prediction displays the same behaviour, but the predictions does not fit at all with stability results for large U^* . Again this range is far from the range of application of the asymptotic theory. Note finally that

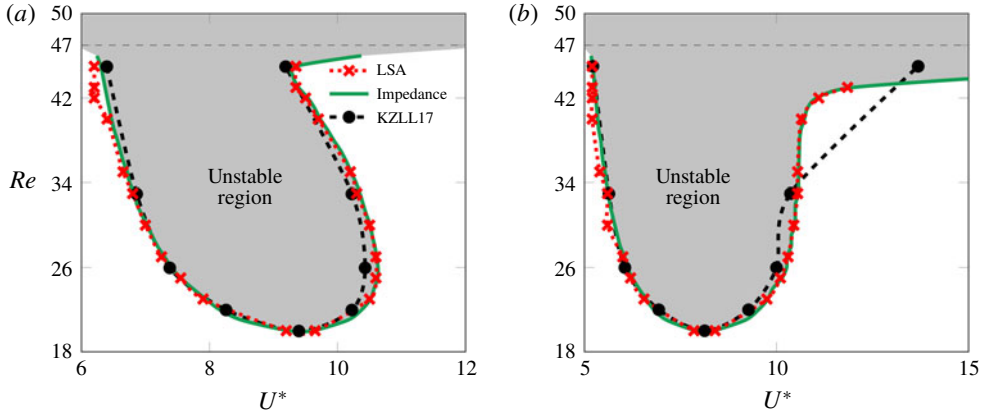


FIGURE 6. The $Re-U^*$ plane distinguishing the region of instability for (a) $m^* = 50$ and (b) $m^* = 4.73$. Results from the current linear stability analysis, the impedance-based predictions, and the coupled cylinder results of Kou *et al.* (2017) (KZLL17).

the asymptotic prediction is multivalued in the range $U^* = [1.304 - 1.355]$. The zoom detail in the plot shows that the threshold obtained at $U^* = 1.270$ (which corresponds to a zero of Z_r) matches with the lower threshold of the stability results, while the two others (which correspond to a change of sign of the real part of the denominator in (3.10)) are incorrect predictions.

6.4. Instability map: $Re-U^*$ plane

The goal of the following section is to identify the stable and unstable zones in the $Re-U^*$ plane, for a fixed mass ratio. By determining the limiting curve where the amplification rate is zero, the region of the parameter space where the cylinder is predicted to vibrate (unstable) can be delineated from the region where the flow is predicted to be steady (stable).

For this purpose, an LSA was carried out over a wide range of reduced velocity U^* , for several values of Re and at a fixed m^* . The values of U^* for which $\omega_i = 0$, for different values of Re , for constant values of $m^* = 50$ and $m^* = 4.73$ are first plotted in figures 6(a) and 6(b), respectively. The results are compared with those from Kou *et al.* (2017) and the impedance-based predictions at the leading order, observing a very good agreement between results. The unstable zone starts at Re_{e3} for lower U^* values and tends to a fixed value when $U^* \rightarrow \infty$. This asymptotic value tends to decrease as m^* decreases. Therefore, for high values of m^* , the curve will tend to Re_{e3} (figure 6a), whereas for low values of m^* , the curve tends to Re_{e2} (figure 6b).

This behaviour is confirmed in figure 7, where the instability threshold is plotted for a very low mass ratio of $m^* = 0.1$. Again, a very close match is observed between the predictions from the linear stability analysis and the impedance-based criterion from the forced case. Also marked on the plot with a dashed line is the value of Re_{e2} , which shows that the threshold for instability approaches this value as U^* increases.

This can be explained by considering that for high masses, the oscillation frequency will be similar to the natural structural frequency, and the imaginary component of the impedance Z_i will have little effect on the value of U^* (as shown in (3.9)) and on the

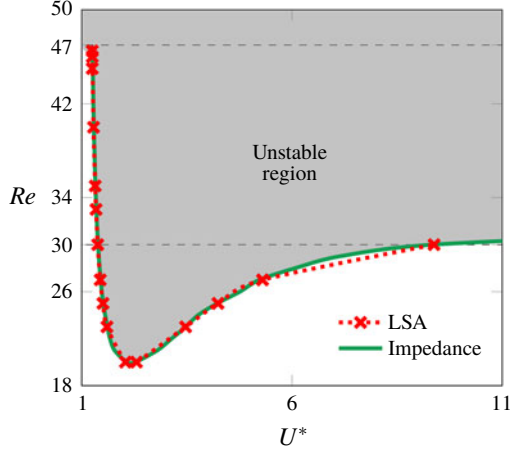


FIGURE 7. Stability threshold for $m^* = 0.1$. Compared are the coupled case results using linear stability analysis and the impedance-based predictions. The grey zone represents the unstable region. The dashed line represents the value of Re_{c2} , showing that at low m^* the instability threshold converges to this value as U^* increases.

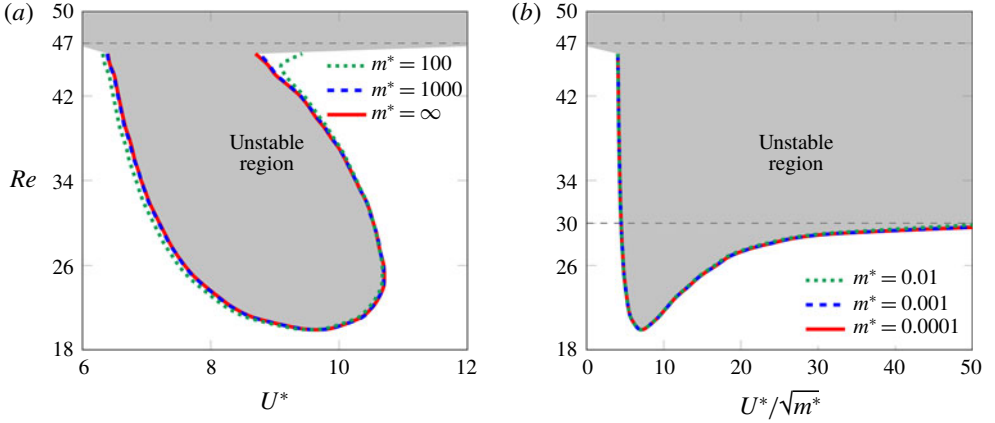


FIGURE 8. Impedance-based results on the threshold instability curve for (a) the case of $m^* \rightarrow \infty$ in the $Re-U^*$ plane, and (b) the case of $m^* \rightarrow 0$ in the $Re-U^*/\sqrt{m^*}$ plane. The grey zones represent the unstable regions.

growth. Conversely for lower m^* , Z_i will impact the dynamics, hence the threshold Re_{c2} where the change of sign of Z_i plays a role. A similar reasoning can be used to explain the influence of the damping ratio γ presented below in § 6.6.

Lastly, the instability threshold curves for the limit cases $m^* \rightarrow \infty$ and $m^* \rightarrow 0$ were computed using the impedance arguments at the leading order and are depicted in figure 8. One can see that for high values of mass ratio, the instability threshold curve tends to be the same in the $Re-U^*$ plane (figure 8a). On the other hand, as m^* tends to zero, a relation in the plane $Re-U^*/\sqrt{m^*}$ is found (figure 8b).

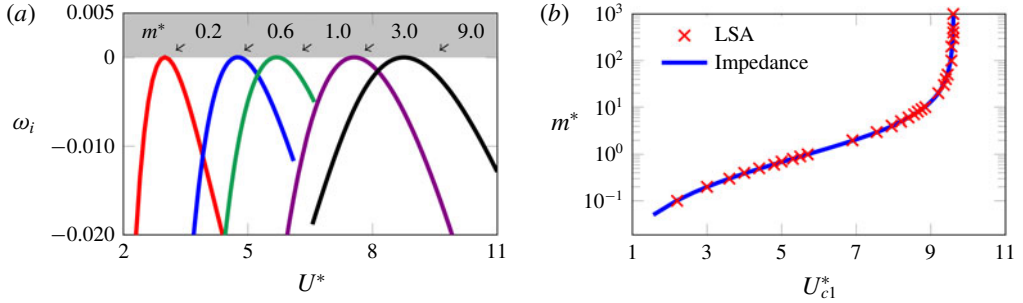


FIGURE 9. (a) Variation of ω_i with U^* for different m^* at $Re_{c1} = 19.946$. The value of m^* is noted above curves in the graphic. The grey zone represents the unstable region. (b) Variation of U_{c1}^* with m^* at $Re_{c1} 19.946$, comparing the values extracted from the turning points of the curves generated via the linear stability analysis, and the prediction from the impedance from the forced oscillation case.

6.5. Instability threshold at $Re \approx 20$

The following analysis is carried out at lower Re , fixing m^* and varying U^* . When decoupled, the eigenvalues associated with the FM always present a negative amplification rate. When coupled, the eigenvalues of one of the modes also obeys this observation (namely the FEM1). The objective is then to determine for which Re the EM (or the other coupled mode, FEM2) presents an eigenvalue with a positive amplification rate and the value of U^* at which this occurs.

The first value of Re for which a positive amplification rate ω_i occurs is $Re = Re_{c1} = 19.946$. Note that this value is very close to the value of $Re_{c1} = 19.915$ predicted via the impedance-based analysis of the linear forced case presented above in § 5.2. Figure 9(a) shows the amplification rate ω_i as a function of U^* for a series of values of m^* for a fixed value of $Re = Re_{c1}$. It is clear that regardless of m^* , there is a value of U^* at the turning point of each curve where the amplification rate is positive and the flow is predicted to be unstable. It is also clear that the value of U^* – here dubbed U_{crit}^* – increases with the increase of the mass ratio. The variation of U_{crit}^* with m^* is compared in figure 9(b) with the impedance-based predictions as defined in (3.9) – the match is almost perfect. Further, the value of U_{c1}^* tends to $U_{c1}^* = 9.605$ as $m^* \rightarrow \infty$, which approaches the value predicted for the natural shedding frequency f_N of the fixed cylinder. Indeed, from figure 3(b) one can see that $f_N = 0.71921/(2\pi) = 0.1145$ at $Re = 40$, which is close to the present critical frequency $f_{c1}^* = 1/9.6048 = 0.1041$.

6.6. Damping factor effect

To this point, all the discussion has been made by supposing $\gamma = 0$. This assumption intuitively sets the amplification rate of the eigenmodes to their highest values, i.e. for the same set of (Re, m^*, U^*) values, the most linearly unstable mode will be the one with $\gamma = 0$. Any value of γ different from zero will damp the system and render it ‘more stable’.

Here this effect is explicitly investigated by examining the effect of the damping factor on the first instability threshold, Re_{c1} . A relationship exists between a mass-damping parameter (the product γm^*) and Re_{c1} for $m^* \gg 1$. This relation is sketched in figure 10 for several mass ratios. For $\gamma = 0$ (or zero damping), all the curves converge to the Re_{c1} discussed in the previous sections. For high values of γ (or γm^*), the

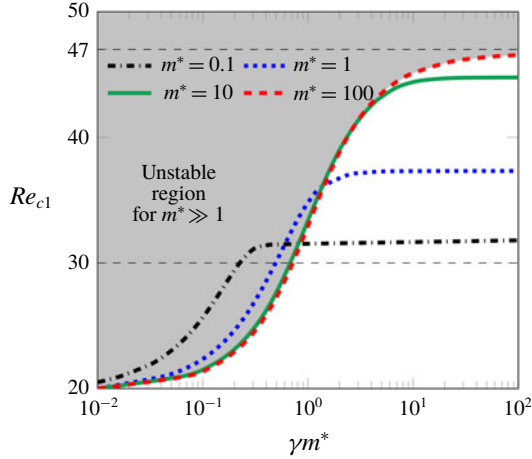


FIGURE 10. The LSA results on the variation of Re_{c1} with the product γm^* for several values of m^* . The grey zone represents the unstable region for $m^* \gg 1$. The horizontal dashed lines indicate the Re_{c2} and Re_{c3} .

threshold tends to a different value of Re depending on the mass ratio, in a similar way as shown for increasing m^* for zero damping as presented in § 6.4. For $m^* \gg 1$, the threshold tends to the value of the fixed-case cylinder, i.e. $Re_{c1} \rightarrow Re_{c3}$. As the mass ratio decreases, the asymptotic value of Re_{c1} also decreases until it reaches the value of Re_{c2} for $m^* \ll 1$, i.e. $Re_{c1} \rightarrow Re_{c2}$. In conclusion, it can be said that the damping removes energy from the system, and hence the instability is only triggered at a higher Re .

7. Conclusions

This paper describes the stability of the flow past an elastically mounted cylinder, focussing on the transition from a steady flow to an unsteady one. Two methods have been described and compared, one using a linear stability analysis of the fully coupled fluid–structure system, and another investigating the energy transfer and its link to impedance when the cylinder motion is harmonically forced.

It has been shown that these two cases are intrinsically linked. The fully coupled system and the harmonically forced system result in the same flow and cylinder motion only when there is zero energy transfer from the flow to the structure and the steady flow is marginally stable. Therefore, the direction of the energy transfer which is linked to the impedance in the forced case can be related to the stability of the flow in the coupled case.

The results show that the instability could be triggered as low as $Re_{c1} \approx 20$ for a specific set of parameters. As Re increases, the unstable zone became wider in terms of U^* range. For low mass ratios, this range had a branch tending to infinity when passing $Re_{c2} \approx 30$. For high mass ratio the singularity appears only at $Re_{c3} \approx 47$. These critical values are well-predicted by the impedance-based analysis. The same reasoning is able to explain the variation of the stability threshold with the damping ratio.

In the vicinity of the marginally stable configurations, the results from the coupled eigenvalue problem can be predicted by an asymptotic development at first order, based on the impedance results from the forced case, either at subcritical or supercritical regimes.

Appendix A. Derivation of the impedance energy relation

This appendix shows the deduction of (3.2). The non-dimensional energy transfer (or mechanical work) from the fluid to the cylinder, over a time interval $[t_1 - t_2]$ can be defined as

$$E_{transfer}(t_1, t_2) = \int_{t_1}^{t_2} [C_y(t)\dot{\zeta}(t)] dt, \quad (\text{A } 1)$$

where $C_y(t)$ is the vertical force coefficient and $\dot{\zeta}(t)$ the instantaneous cylinder vertical velocity. Suppose a normal form for $C_y(t)$ and $\zeta(t)$ as presented in (2.6). Let $(|\hat{\zeta}|, \theta)$ and $(|\hat{C}_y|, \theta + \phi)$ represent the magnitude and argument of $\hat{\zeta}$ and \hat{C}_y , respectively, where θ is the phase of $\zeta(t)$ and ϕ is the phase angle between the vertical force coefficient and the cylinder vertical displacement. Equation (2.6) can be rearranged and written as

$$C_y(t) = C_{y,h}(t) e^{\omega_i t} \quad \text{with} \quad C_{y,h}(t) = |\hat{C}_y| \cos(\omega_r t + \theta + \phi), \quad (\text{A } 2a)$$

$$\zeta(t) = \zeta_h(t) e^{\omega_i t} \quad \text{with} \quad \zeta_h(t) = |\hat{\zeta}| \cos(\omega_r t + \theta), \quad (\text{A } 2b)$$

where the (\bullet_h) subscript identifies the sinusoidal component of the instantaneous signal. Using the former expressions of $C_y(t)$ and $\zeta(t)$, the energy equation (A 1) can be expanded as

$$E_{transfer}(t_1, t_2) = \int_{t_1}^{t_2} [C_{y,h}(t) e^{\omega_i t} (\dot{\zeta}_h(t) e^{\omega_i t} + \zeta_h(t) \omega_i e^{\omega_i t})] dt, \quad (\text{A } 3)$$

or

$$\begin{aligned} E_{transfer}(t_1, t_2) = & - \int_{t_1}^{t_2} [|\hat{C}_y| |\hat{\zeta}| (\omega_r \cos(\omega_r t + \theta + \phi) \sin(\omega_r t + \theta))] e^{2\omega_i t} dt \\ & + \int_{t_1}^{t_2} [|\hat{C}_y| |\hat{\zeta}| (\omega_i \cos(\omega_r t + \theta + \phi) \cos(\omega_r t + \theta))] e^{2\omega_i t} dt. \end{aligned} \quad (\text{A } 4)$$

If the non-dimensional energy transfer over a time period of the cylinder oscillation $T_{cycle} = 2\pi/\omega_r$ is now considered, then $t_2 = t_1 + T_{cycle}$. If one excludes the exponential growth/decay of the eigenmode, characterising only a harmonic motion, equation (A 4) is reduced to

$$E_{transfer,h} \equiv E_{transfer}(t_1, t_1 + T_{cycle}) \equiv \int_{t_1}^{t_1 + T_{cycle}} [C_{y,h}(t)\dot{\zeta}_h(t)] dt = -\pi |\hat{C}_y| |\hat{\zeta}| \sin(\phi). \quad (\text{A } 5)$$

The latter equation shows the important role of the phase angle ϕ in the control of the energy transfer between the fluid and the structure. When the coupled cylinder oscillations have achieved a fully developed state, the energy transferred from the fluid to the cylinder matches the energy dissipated by the structural damping. If one considers the structural damping to be zero, energy transfer in the limit cycle is also zero. Thus, the value of ϕ can either be 0° or 180° for the coupled case cylinder (Morse & Williamson 2009b; Navrose & Mittal 2016).

The impedance concept, introduced in § 2.3.1 and applied to a general case, reads $Z = -\hat{C}_y/\hat{\zeta}$. Developing the former formula, one arrives to a real and an imaginary part of the impedance given by

$$Z_r = -\frac{|\hat{C}_y|}{(\omega_i^2 + \omega_r^2)|\hat{\zeta}|} (\omega_i \cos \phi - \omega_r \sin \phi) \quad \text{and} \quad Z_i = -\frac{|\hat{C}_y|}{(\omega_i^2 + \omega_r^2)|\hat{\zeta}|} (\omega_i \sin \phi + \omega_r \cos \phi). \quad (\text{A } 6a,b)$$

For a harmonic motion, where $\omega_i = 0$, one will have $\omega_r \equiv \omega_F$ and

$$Z_r(\omega_F) = \frac{|\hat{C}_y|}{\omega_F |\hat{\zeta}|} \sin \phi \quad \text{and} \quad Z_i(\omega_F) = -\frac{|\hat{C}_y|}{\omega_F |\hat{\zeta}|} \cos \phi. \quad (\text{A } 7a,b)$$

Introducing the $Z_r(\omega_F)$ expression on (A 5), one arrives at the expression for the energy transfer over one cycle of oscillation of the purely harmonic case

$$E_{transfer,h} = -\pi |\hat{\zeta}|^2 \omega_F Z_r(\omega_F), \quad (\text{A } 8)$$

as presented in (3.2) of the present manuscript.

Appendix B. Detail on the linearised Navier–Stokes equations

B.1. Base flow equations

The equations for the base flow are obtained by inserting time-independent state variable $\mathbf{q}_b = (\mathbf{u}_b, p_b)^\top$ into the Navier–Stokes equations

$$-\frac{1}{2} \mathcal{C}(\mathbf{u}_b, \mathbf{u}_b) - \nabla p_b + 2Re^{-1} \nabla \cdot \mathbf{D}(\mathbf{u}_b) = 0, \quad (\text{B } 1a)$$

$$\nabla \cdot \mathbf{u}_b = 0, \quad (\text{B } 1b)$$

where $\mathcal{C}(\mathbf{u}_b, \bullet) := (\mathbf{u}_b \cdot \nabla) \bullet + (\bullet \cdot \nabla) \mathbf{u}_b$ is the convection operator. For this problem, the boundary conditions are defined as

$$\mathbf{u}_b = 0 \quad \text{on } \Gamma_{cy}, \quad (\text{B } 2a)$$

$$\mathbf{u}_b = U_\infty \hat{\mathbf{i}} \quad \text{on } \Gamma_{in} \cup \Gamma_{lat}, \quad (\text{B } 2b)$$

$$[-\nabla p_b + 2Re^{-1} \mathbf{D}(\mathbf{u}_b)] \cdot \mathbf{n} = 0 \quad \text{on } \Gamma_{out}, \quad (\text{B } 2c)$$

$$\mathbf{u}_b \cdot \hat{\mathbf{j}} = 0 \wedge \nabla \mathbf{u}_b \cdot \hat{\mathbf{j}} = 0 \quad \text{on } \Gamma_{axis}. \quad (\text{B } 2d)$$

B.2. Perturbation equations

The equations governing the perturbation $\hat{\mathbf{q}}$ are obtained by setting $\mathbf{q} = \mathbf{q}_b + \epsilon(\hat{\mathbf{q}} \exp(-i\omega t) + \text{c.c.})/2$ in the Navier–Stokes equations and linearising. The cylinder motion is also taken as $\hat{\zeta} = \epsilon(\hat{\zeta} \exp(-i\omega t) + \text{c.c.})/2$. This leads to

$$-i\omega \hat{\mathbf{u}} + \mathcal{C}(\mathbf{u}_b, \hat{\mathbf{u}}) - 2Re^{-1} \nabla \cdot \mathbf{D}(\hat{\mathbf{u}}) + \nabla \hat{p} = (\hat{\zeta} \hat{\mathbf{j}} \cdot \nabla) \mathbf{u}_b, \quad (\text{B } 3a)$$

$$\nabla \cdot \hat{\mathbf{u}} = 0, \quad (\text{B } 3b)$$

with boundary conditions

$$\hat{\mathbf{u}} = -\hat{\zeta} \hat{\mathbf{j}} \quad \text{on } \Gamma_{cy}, \quad (\text{B } 4a)$$

$$\hat{\mathbf{u}} = 0 \quad \text{on } \Gamma_{in} \cup \Gamma_{lat}, \quad (\text{B } 4b)$$

$$[-\nabla \hat{p} + 2Re^{-1} \mathbf{D}(\hat{\mathbf{u}})] \cdot \mathbf{n} = 0 \quad \text{on } \Gamma_{out}, \quad (\text{B } 4c)$$

$$\hat{\mathbf{u}} \cdot \hat{\mathbf{i}} = 0 \quad \text{on } \Gamma_{axis}. \quad (\text{B } 4d)$$

B.3. Weak formulation

To set these equations to a form amenable to numerical resolution using a finite-element method, the test functions \mathbf{u}^o , p^o are introduced, associated with the velocity and pressure. Equations (B 3a) and (B 3b) are multiplied by \mathbf{u}^o and p^o , respectively, and integrated over the domain. The Dirichlet boundary conditions are incorporated by penalisation, i.e. by multiplying $\mathbf{u}^o \cdot \hat{\mathbf{u}}$ by $1/\epsilon$ and integrating along the corresponding boundaries. The Neumann boundary conditions are naturally taken into account by the finite-element formulation. After integration by parts of the pressure and viscous stress terms, this leads to a weak form of the equations that can be defined, for the forced problem, as

$$\forall \mathbf{q}^o = (\mathbf{u}^o, p^o)^T, \quad \mathbf{A}_{ff}(\hat{\mathbf{q}}_F, \mathbf{q}^o) - i\omega_F \mathbf{B}_{ff}(\hat{\mathbf{q}}_F, \mathbf{q}^o) = \hat{\zeta}_F \mathbf{Y}(\mathbf{q}^o), \quad (\text{B } 5)$$

where the bilinear operators \mathbf{A}_{ff} and \mathbf{B}_{ff} and the linear operator \mathbf{Y} are defined as follows:

$$\begin{aligned} \mathbf{A}_{ff}(\hat{\mathbf{q}}_F, \mathbf{q}^o) &= \int_{\Omega} [C(\mathbf{u}_b, \hat{\mathbf{u}}_F) \cdot \mathbf{u}^o + 2Re^{-1} \mathbf{D}(\hat{\mathbf{u}}_F) : \mathbf{D}(\mathbf{u}^o) - \hat{p}_F \nabla \cdot \mathbf{u}^o \\ &\quad + p^o \nabla \cdot \hat{\mathbf{u}}_F] \, d\Omega \\ &\quad + \frac{1}{\epsilon} \int_{\Gamma_{cy} \cup \Gamma_{in} \cup \Gamma_{lat}} \mathbf{u}^o \cdot \hat{\mathbf{u}}_F \, d(\Gamma_{cy} \cup \Gamma_{in} \cup \Gamma_{lat}) \\ &\quad + \frac{1}{\epsilon} \int_{\Gamma_{ax}} u_x^o \hat{u}_{x,F} \, d\Gamma_{ax}, \end{aligned} \quad (\text{B } 6a)$$

$$\mathbf{B}_{ff}(\hat{\mathbf{q}}_F, \mathbf{q}^o) = \int_{\Omega} \hat{\mathbf{u}}_F \cdot \mathbf{u}^o \, d\Omega, \quad (\text{B } 6b)$$

$$\mathbf{Y}(\mathbf{q}^o) = \int_{\Omega} u_y^o \hat{\mathbf{j}} \cdot \nabla \mathbf{u}_b - \frac{1}{\epsilon} \int_{\Gamma_{cy}} u_y^o \hat{\mathbf{j}}. \quad (\text{B } 6c)$$

These operators are also used for defining the coupled problem, as presented in (2.9) and (2.10). This is followed by the spatial discretisation, described in § 4.

Finally, the ‘vertical force coefficient’ operator is defined as

$$\mathbf{L}(\hat{\mathbf{q}}) = 4 \int_{\Gamma_{cy}} \{(-pn + 2Re^{-1} \mathbf{D}(\mathbf{u}) \cdot \mathbf{n}) \cdot \hat{\mathbf{j}}\} \, d\Gamma_{cy}. \quad (\text{B } 7)$$

REFERENCES

- BEARMAN, P. W. 2011 Circular cylinder wakes and vortex-induced vibrations. *J. Fluids Struct.* **27** (5), 648–658.
- BISHOP, R. & HASSAN, A. 1964 The lift and drag forces on a circular cylinder oscillating in a flowing fluid. *Proc. R. Soc. Lond.* **277**, 51–75.
- BREZZI, F. & FORTIN, M. 1991 *Mixed and Hybrid Finite Element Methods*. Springer.
- BUFFONI, E. 2003 Vortex shedding in subcritical conditions. *Phys. Fluids* **15** (3), 814–816.
- CONCIAURO, G. & PUGLISI, M. 1981 Meaning of the negative impedance. *NASA STI/Recon Tech. Rep. N* 82.
- COSSU, C. & MORINO, L. 2000 On the instability of a spring-mounted circular cylinder in a viscous flow at low Reynolds numbers. *J. Fluids Struct.* **14** (2), 183–196.
- DUŠEK, J., LE GAL, P. & FRAINIEÉ, P. 1994 A numerical and theoretical study of the first Hopf bifurcation in a cylinder wake. *J. Fluid Mech.* **264**, 59–80.

- FABRE, D., ASSEMAT, P. & MAGNAUDET, J. 2011 A quasi-static approach to the stability of the path of heavy bodies falling within a viscous fluid. *J. Fluids Struct.* **27** (5), 758–767.
- FABRE, D., CITRO, V., FERREIRA SABINO, D., BONNEFIS, P., SIERRA, J., GIANNETTI, F. & PIGOU, M. 2018 A practical review on linear and nonlinear global approaches to flow instabilities. *Appl. Mech. Rev.* **70**, 060802.
- FABRE, D., LONGOBARDI, R., CITRO, V. & LUCHINI, P. 2020 Acoustic impedance and hydrodynamic instability of the flow through a circular aperture in a thick plate. *J. Fluid Mech.* **885**, A11.
- FENG, C. C. 1968 The measurement of vortex induced effects in flow past stationary and oscillating circular and d-section cylinders. PhD thesis, The University of British Columbia, Canada.
- GIANNETTI, F. & LUCHINI, P. 2007 Structural sensitivity of the first instability of the cylinder wake. *J. Fluid Mech.* **581**, 167–197.
- GRIFFIN, O. M., SKOP, R. A. & KOOPMANN, G. H. 1973 The vortex-excited resonant vibrations of circular cylinders. *J. Sound Vib.* **31** (2), 235–249.
- HECHT, F. 2012 New development in FreeFem++. *J. Numer. Math.* **20** (3–4), 251–265.
- KARNIADAKIS, G. & SHERWIN, S. 2005 *Spectral/hp Element Methods for Computational Fluid Dynamics*. Oxford University Press.
- KARNIADAKIS, G. E. & TRIANTAFYLLOU, G. S. 1989 Frequency selection and asymptotic states in laminar wakes. *J. Fluid Mech.* **199**, 441–469.
- KOU, J., ZHANGA, W., LIU, Y. & LI, X. 2017 The lowest Reynolds number of vortex-induced vibrations. *Phys. Fluids* **29**, 041701.
- LEONTINI, J. S., GRIFFITH, M. D., LO JACONO, D. & SHERIDAN, J. 2018 The flow-induced vibration of an elliptical cross-section at varying angles of attack. *J. Fluids Struct.* **78**, 356–373.
- LEONTINI, J. S., STEWART, B. E., THOMPSON, M. C. & HOURIGAN, K. 2006a Wake state and energy transitions of an oscillating cylinder at low Reynolds number. *Phys. Fluids* **18** (6), 067101.
- LEONTINI, J. S., THOMPSON, M. C. & HOURIGAN, K. 2006b The beginning of branching behaviour of vortex-induced vibration during two-dimensional flow. *J. Fluids Struct.* **22** (6–7), 857–864.
- MELIGA, P. & CHOMAZ, J. M. 2011 An asymptotic expansion for the vortex-induced vibrations of a circular cylinder. *J. Fluid Mech.* **671**, 137–167.
- MITTAL, S. & SINGH, S. 2005 Vortex-induced vibrations at subcritical Re. *J. Fluid Mech.* **534**, 185–194.
- MORSE, T. L. & WILLIAMSON, C. H. K. 2006 Employing controlled vibrations to predict fluid forces on a cylinder undergoing vortex-induced vibration. *J. Fluids Struct.* **22** (6), 877–884.
- MORSE, T. L. & WILLIAMSON, C. H. K. 2009a Fluid forcing, wake modes, and transitions for a cylinder undergoing controlled oscillations. *J. Fluids Struct.* **25** (4), 697–712.
- MORSE, T. L. & WILLIAMSON, C. H. K. 2009b Prediction of vortex-induced vibration response by employing controlled motion. *J. Fluid Mech.* **634**, 5–39.
- MOUGIN, G. & MAGNAUDET, J. 2002 The generalized Kirchhoff equations and their application to the interaction between a rigid body and an arbitrary time-dependent viscous flow. *Intl J. Multiphase Flow* **28** (11), 1837–1851.
- NAVROSE & MITTAL, S. 2016 Lock-in in vortex-induced vibration. *J. Fluid Mech.* **794**, 565–594.
- PARKINSON, G. 1989 Phenomena and modelling of flow-induced vibrations of bluff bodies. *Prog. Aerosp. Sci.* **26** (2), 169–224.
- PROVANSAL, M., MATHIS, C. & BOYER, L. 1987 Bénard–von Kármán instability: transient and forced regimes. *J. Fluid Mech.* **182**, 1–22.
- THOMPSON, M. C., HOURIGAN, K. & SHERIDAN, J. 1996 Three-dimensional instabilities in the wake of a circular cylinder. *J. Expl Therm. Fluid Sci.* **12** (2), 190–196.
- WILLIAMSON, C. H. K. & GOVARDHAN, R. 2004 Vortex-induced vibrations. *Annu. Rev. Fluid Mech.* **36**, 413–455.
- WILLIAMSON, C. H. K. & ROSHKO, A. 1988 Vortex formation in the wake of an oscillating cylinder. *J. Fluids Struct.* **2** (4), 355–381.
- ZHANG, W., LI, X., YE, Z. & JIANG 2015 Mechanism of frequency lock-in in vortex-induced vibrations at low Reynolds numbers. *J. Fluid Mech.* **783**, 72–102.